

Melting transition of confined Lennard-Jones solids in slit pores

Chandan K. Das · Jayant K. Singh

Received: 11 September 2012 / Accepted: 8 February 2013 / Published online: 28 February 2013
© Springer-Verlag Berlin Heidelberg 2013

Abstract The melting transition of a Lennard-Jones (LJ) system confined in slit pores of variable pore size, H , is studied using molecular dynamics simulations. We examine various mechanisms to locate the pore melting temperature under confinement using molecular simulations. Three types of structure-less pore walls are considered, namely strongly attractive walls, weakly attractive walls, and repulsive walls. In particular, we present details of the density–temperature hysteresis, Lindemann parameter, and non-Gaussian parameter for various pore sizes ranging from 8 to 3 molecular diameters. The methods as used in this work are found applicable for repulsive, weak, and moderately attractive pores. Using the above criteria, we estimated the melting temperature for various pore surfaces and pore sizes. The melting temperature, for an attractive surface, is observed to be elevated or depressed depending on the pore size. In contrast, depression in the melting temperature is observed in the case of weakly attractive and repulsive surfaces. Crossover behavior from three-dimensional to two-dimensional for weakly attractive and repulsive surfaces is proposed using the relation $\Delta T_m \sim H^{-\nu}$, with ν ranging from 0.66 to 0.81 and 1.59 to 2.1 for 2D and 3D, respectively. The methods, viz., Lindemann and non-Gaussian parameters, however, fail in predicting melting temperature for $\epsilon_{wf} > 8$ and $\alpha > 4$ for LJ 6-12 and LJ 9-3, surfaces, respectively.

Keywords Melting · Confined solids · Molecular dynamics · Lindemann parameter · Non-Gaussian parameter

1 Introduction

Melting, the phenomenon of phase transition from a crystalline solid state to a liquid state, is a common occurrence in nature. Since the dawn of industrial development, investigations of the melting of solids have been of importance for science and technology. As one of the most important phase transformations in the processing and applications of materials, the melting process plays an important role in materials science and engineering [1]. Furthermore, the melting of solids is important in the natural environment, biology, and many other fields. In recent years, a greater attention has been given for studying melting/freezing phenomena in confinement. The physics behind confined systems plays a vital role in various fields of modern technology such as microfluidics, lubrication, adhesion, and nanotechnology [2]. The conformation of a system is changed in confinement, and depends on the scale of the confinement and the nature of the confined surface. Therefore, the properties of a confined system are different from those of bulk systems.

Several experimental studies have been reported on melting and freezing in well-characterized porous materials [3–5]. Studies on porous Vycor glass show a lowering of the melting point compared to that in the bulk. The melting point of the confined solid also depends on the attractive or repulsive natures of surfaces, and the hysteresis associated with the transition [6, 7]. For example, on narrowing the channel size of a colloidal suspension system (confined in a flat channel), the system behavior changes from three-

Published as part of the special collection of articles derived from the conference: Foundations of Molecular Modeling and Simulation 2012.

C. K. Das · J. K. Singh (✉)
Department of Chemical Engineering, Indian Institute of
Technology Kanpur, Kanpur 208016, India
e-mail: jayantks@iitk.ac.in

dimensional (3D) to two-dimensional (2D) behavior, and a colloidal monolayer system displays continuous 2D melting [8–11]. Lowering of the freezing temperature, based on the Gibbs–Thomson thermodynamic equation, is observed for oxygen in sol–gel glasses of pore size distribution 2.2–18.7 nm [12]. Because of the presence of inhomogeneity and finite size effects for small pore sizes, this thermodynamic relationship does not hold. Large effects on the freezing and melting temperatures of indium in porous silica glasses have also been reported [4]. In contrast to these results for glasses, some other experiments have identified a significant increase in the melting temperatures of cyclohexane and octamethylcyclotetrasiloxane confined between mica surfaces, using a surface force apparatus [5]. In certain confined cases, liquids are fluid down to a film thickness of a few molecular layers. On further reducing the wall separation by a single molecular layer, the films experience an abrupt transition, becoming solid-like, and can sustain a finite shear stress for macroscopic times. This is familiar as surface-induced phase transitions from liquid-like to solid-like [5, 13, 14].

Molecular simulation studies are also useful for investigating such processes. The homogeneous and heterogeneous melting phenomena of different metals with different crystalline structures have been discussed in light of different melting mechanisms [15–17]. The freezing transition and phase diagrams of hard sphere confined in hard slit and cylindrical pores have been discussed using molecular simulations [18] and free-volume theory [19]. Miyahara and Gubbins reported the freezing of a Lennard-Jones (LJ) solid under confinement [20]. Considering the slit pore geometry, they showed a decrease in freezing point with decreasing slit separation. They also reported that the elevation/depression in the freezing point depends on the strength of the wall–fluid interaction, and the width of the hysteresis also depends on the nature of the surfaces. They did not find any kind of phase transition or hysteresis loop for a pore size of $H < 5$ molecular diameters. Depression in the freezing point is also observed in weakly attractive cylindrical pores of diameter 1.5–3.5 nm [21]. Evidence of transition from a 2D liquid phase to a hexatic phase is observed for simple fluids in narrow slit pores [22]. Both experimental and simulation studies of fluids confined in cylindrical silica pores (involving free-energy calculations) suggest that for pore diameters smaller than 20 molecular diameters, the confined phase does not crystallize into a homogeneous solid phase, and for diameters smaller than 12 molecular diameters, the confined solid phase was amorphous throughout the pores [23]. In case of mixtures, both an increase and a decrease in the freezing temperature are observed, depending on the mole fractions of the components [24]. The freezing/melting behaviors of confined fluids have been reported to be related to variations in

the ratio of wall–fluid and fluid–fluid interactions [25, 26]. Recently, Kaneko et al. [27] performed molecular dynamics (MD) simulations of LJ particles confined in parallel slit pores with widths from 2 to 6 molecular diameters. The authors estimated the freezing/melting point when the LJ fluid was cooled/heated by observing sudden jumps in the potential energy and density, and observed an abnormality in the freezing/melting point corresponding to differences in the crystal structure; the results were in good agreement with calculations using the Clausius–Clapeyron equation for the slit system [28].

Bulk melting/freezing phenomena have been reported by many simulation groups. Most of the work is based on the Lindemann parameter (bulk) [29, 30], Born criteria (bulk) [31], non-Gaussian parameter (bulk) [29], static order parameter [17], free-energy calculations [21, 25, 32], structure factor [20, 33–36], radial distribution function, and orientational correlation function [21, 23].

Although these theories and criteria have been successfully implemented for bulk systems, they are of limited application for freezing and melting in confined systems. Miyahara and Gubbins [20] successfully used a *structure factor* criterion to determine the freezing temperature under confinement. Radhakrishnan et al. [23, 26] summarized the differences between the freezing/melting temperatures in a confined system and that of a bulk system on the basis of the Landau free energy, radial distribution function, and orientational correlation function. Earlier studies [5, 12, 20, 22, 27, 32] showed that elevation and depression in melting/freezing temperatures are more or less linearly related to the inverse of the pore gap. Mostly their attentions were limited to freezing transition on quenching the system. Moreover, most of the earlier studies were reported based on positional/orientational correlation function. Recent work of Kaneko et al. [27], based on cooling/heating simulations, reports an oscillatory behavior of melting and freezing temperatures with pore size and casted doubt on the earlier believed linear nature of the melting/freezing temperature with decreasing pore size. Motivated from the aforementioned result, this work aims to provide more clarity in the nature of melting behavior of confined solids from a different approach.

In this work, we first analyze density hysteresis loop, Lindemann parameter, and non-Gaussian parameter for evaluating the melting temperatures of confined fluids. We present the melting temperature of an LJ solid for slit separations (pore sizes) ranging from 8 to 3 molecular diameters. Further, we investigate the role of surface affinity on the melting temperature. The rest of the paper is organized as follows. The model and method are described in Sect. 2. In Sect. 3, some details of the simulations are provided, and in Sect. 4, the results are presented and discussed. Finally, concluding remarks are presented in Sect. 5.

2 Model and methods

2.1 Potential models

For fluid–fluid interactions, the LJ potential is used in the following form:

$$U_{ff}(r) = 4\epsilon_{ff} \left[\left(\frac{\sigma_{ff}}{r} \right)^{12} - \left(\frac{\sigma_{ff}}{r} \right)^6 \right], \quad (1)$$

where σ_{ff} is the particle diameter, ϵ_{ff} is the interaction well depth, and r is the distance between two corresponding particles. All quantities are reduced with respect to ϵ_{ff} and σ_{ff} , that is, these LJ parameters are fixed to unity.

In this work, the pore is modeled as a slit pore with structure-less walls. Interactions between the walls and fluid particles are the same as the LJ (12–6) potential. In the case of a weakly interactive wall, we use a potential well depth $\epsilon_{wf} = 1$, and for a moderate attractive wall, the potential well depth is $\epsilon_{wf} = 3$. The diameter of the wall particle is considered to be of the same order as the system particles.

For stronger wall-particle interaction, we also use the integrated form of LJ (12–6) potential, that is, LJ 9–3 potential [7]. The potential form is as follows:

$$U_{wf}(r) = \frac{2}{3} \pi \rho_w \epsilon_{wf} \sigma_{wf}^3 \left[\frac{2}{15} \left(\frac{\sigma_{wf}}{r} \right)^9 - \left(\frac{\sigma_{wf}}{r} \right)^3 \right], \quad (2)$$

where ρ_w is the number density of atoms in the wall and σ_{wf} and ϵ_{wf} are the cross parameters for the wall–fluid interaction. In this work, we fix $\sigma_{ff} = 1$, $\epsilon_{ff} = 1$, $\sigma_{ww} = 0.8924$, $\rho_w = 6.3049$, $\sigma_{wf} = (\sigma_{ff} + \sigma_{ww})/2$ as per Ref. [7] and [20]. The strength of interaction of the wall–fluid relative to fluid–fluid interaction is defined by the coefficient, $\alpha = \rho_w \epsilon_{wf} \sigma_{wf}^3 / \epsilon_{ff}$. In this work, we change ϵ_{wf} to vary α , keeping all other parameters fixed.

For a repulsive wall, we use the Weeks–Chandler–Anderson (WCA) potential, which is a purely repulsive interaction potential. The potential is formed by truncating the LJ (12–6) potential at $2^{1/6}\sigma$ and shifted upward so that it goes to zero smoothly at the cutoff radius. The potential form is as follows:

$$U_{wf}(r) = 4\epsilon_{wf} \left[\left(\frac{\sigma}{r} \right)^{12} - \left(\frac{\sigma}{r} \right)^6 \right], \quad r < 2^{1/6}\sigma \quad (3)$$

Fluid–fluid potential model is truncated and shifted at 3.0σ . In case of soft wall potentials, that is, LJ 6–12 and LJ 9–3, the potential models are also truncated and shifted at 3σ .

2.2 Simulation methodologies

There are thermodynamic routes for evaluating the true freezing/melting temperature, which are summarized by

Monson and Kofke [37]. In this work, we adopt a different route, based on the Lindemann parameter and the non-Gaussian parameter, to locate the melting temperature. These parameters are very temperature sensitive particularly near the melting temperature. Hence, the computed melting temperature using the Lindemann and non-Gaussian parameters is considered to be relatively more accurate than those obtained using other melting criteria such as the Born [31] or Hansen–Verlet [33] criteria.

2.2.1 Lindemann parameter

The Lindemann criterion [38] is widely used to determine the melting temperature of a solid; it states that melting is a vibrational lattice instability initiated when the root-mean-square (RMS) displacement of atoms reaches a critical fraction of the interatomic distance:

$$\sqrt{\langle \Delta r^2 \rangle} = \delta_L a \quad (4)$$

where δ_L is the Lindemann parameter, a is the nearest neighbor distance, and $\Delta r = |r_i(t) - R_i|$; r_i is the instantaneous position of atom i and R_i is the equilibrium position of atom i . The nearest neighbor distance can be considered as the position of the first peak of the radial distribution function. The value of the Lindemann parameter for the melting of bulk face-centered cubic (FCC) crystals is 0.22 and for body-centered cubic (BCC) crystals it is 0.18 [7, 29, 39, 40].

2.2.2 Non-Gaussian parameter

Large deviations of solid particles near the melting temperature can be expressed using the non-Gaussian parameter, which is a simple correlation of the second and fourth moments of a 3D distribution in the form $\Delta r[= |r_i(t) - R_i|]$ with time t . The non-Gaussian parameter is defined as:

$$\alpha_2(t) = \frac{3\langle \Delta r^4 \rangle}{5\langle \Delta r^2 \rangle^2} - 1 \quad (5)$$

The value of $\alpha_2(t)$ is very small and is weakly dependent on temperature at lower temperatures. At a certain temperature, $\alpha_2(t)$ suddenly jumps as a result of the strong deviation of atoms from their equilibrium lattice position. This is an indication of the melting temperature. Subsequently, $\alpha_2(t)$ drops to zero, indicating complete loss of crystallinity in a random liquid [29]. The non-Gaussian parameter can also be used to detect the melting point of a solid, as shown by Jin et al. [29].

2.2.3 In-plane pair correlation function and coordination number

The in-plane correlation function is typically used to analyze the structure and phase of a confined molecular system. The in-plane pair correlation function, or in-plane radial distribution function, can be estimated for each layer of a confined liquid/solid using the following expression:

$$g_i(r) = \frac{A(z_{i-1} - z_i)}{2\pi\Delta r(z_{i-1} - z_i)} \frac{\langle N(r; z_{i-1}, z_i) \rangle}{\langle N(z_{i-1}, z_i) \rangle} \quad (6)$$

$$= \frac{\langle N(r; z_{i-1}, z_i) \rangle}{2\pi r \Delta r \Gamma_i},$$

where $A(z_{i-1}-z_i)$ is the cross-sectional area and $N(r; z_{i-1}, z_i)$ indicates the total number of particles at a distance between $r - \Delta r/2$ and $r + \Delta r/2$ in the i th layer between z_{i-1} and z_i . Γ_i is the 2D density. The average number of neighbors, N_c , in the 2D plane, up to a distance r_c , the first minimum of the in-plane pair correlation function (first coordination shell), is evaluated from the in-plane correlation function using the following formula:

$$N_c = 2\pi \frac{N}{V} \int_0^{r_c} r g(r) dr \quad (7)$$

The nearest neighbor distance, a , calculated from the in-plane pair correlation function, can be used to calculate the Lindemann parameter using Eq. (4).

2.2.4 In-plane structure factor

The structure factor is also used as a freezing/melting transition criterion in the bulk phase. According to Hansen and Verlet [33], freezing/melting occurs when $S(k_0)$, the first peak of the structure factor, reaches a value of 2.7 for quenching/heating, respectively.

For a 2D system, the structure factor $S(k)$ is also an important criterion for freezing and melting. The value of $S(k_0)$ for a 2D system is higher than the bulk value. The value is around 4.4–5.0, as reported in earlier studies [34–36, 41]. These results are for purely 2D systems.

In general, the structure factor for a 3D system is defined as:

$$S(k) = 4\pi\rho \int_0^\infty J_0(kr)(g(r) - 1)r^2 dr \quad (8)$$

For 2D systems, the formula is:

$$S(k) = 1 + 2\pi\Gamma_N \int_0^\infty J_0(kr)(g_N(r) - 1)r dr \quad (9)$$

where J_0 is the zeroth-order Bessel function of the first kind.

2.2.5 In-plane order parameter

Changes in the crystal structure with slit separation can also be analyzed using bond-order parameters. We calculated the in-plane bond-order parameter in the following manner for each layer from the MD configuration data:

$$\Psi_k = \left\langle \frac{1}{N_b} \left| \sum_{j=1}^{N_b} \exp(ik\theta_j) \right|^2 \right\rangle \quad (10)$$

where N_b is the total number of near neighbors at a distance of 1.5 in each layer, θ_j is the angle formed by a particle with its nearest neighbor atom. We calculated Ψ_4 and Ψ_6 . $\Psi_k = 1$ indicates that there is complete k -time symmetry in the layer and $\Psi_k = 0$ means there is no symmetry at all in the layer. A high value of Ψ_4 indicates square symmetry in the plane and of Ψ_6 indicates triangular symmetry.

3 Simulation details

The NPT MD is performed using LAMMPS [42]. The velocity-Verlet algorithm is used to integrate the equation of motion with a time step (ΔT) of 0.004. The temperature and pressure are controlled using a Nosé–Hoover thermostat and barostat with relaxation times of 2.0 and 5.0 for temperature and pressure, respectively. In the current work, the model fluid is confined between two structure-less parallel slit surfaces separated by a distance H . H is varied from 3 to 8 molecular diameters. Approximately 4,000–7,200 particles are used to run the simulations. Wall–particle interactions are the same as the particle–particle interactions described in the potential section, IIA. The periodic boundary condition is applied in two directions other than the fixed wall direction. We maintain a constant pressure $P = 1$ along the periodic boundary directions. Similar methodology has been adopted by earlier workers [27, 43]. In the case of quenching, the initial liquid configurations are taken as perfect FCC structures at a temperature of 1.2. Cooling is performed in a step-by-step procedure after each 2,500,000 MD time steps; the temperature T is reduced in steps of 0.05 from 1.2 to 0.3. During the heating process, we have taken the last configuration of the quenching process as the initial configuration. Heating is also performed using a step-by-step procedure. After 2,500,000 MD time steps, the temperature T is increased by 0.05, and heating is continued until the solid has completely lost its crystallinity. During both quenching and heating cycle, the density is calculated at every temperature. In addition, we separately perform

another simulation to determine the melting temperature of the bulk LJ system.

For the Lindemann parameter (δ_L) and non-Gaussian parameter ($\alpha_2(t)$), an additional NPT simulation is carried out with temperature increases in 0.00042 after each 2,500 MD time steps, according to Jin et al. [29], from an initial temperature of 0.3 to a final temperature of 1.2; the rest of the procedure is as described earlier. At every intermediate temperature, we calculate the Lindemann parameter and non-Gaussian parameter.

4 Results and discussion

4.1 Weakly interacting surface

We start our discussion with the weakly interactive LJ 12-6 wall case, with $\varepsilon_{wf} = 1$. Figure 1 shows a plot of the density against the temperature for quenching and heating cases. As the liquid is quenched, the density gradually increases and at a certain temperature the density rises sharply. In the case of heating, the density decreases and at a particular temperature the density drops sharply. The hysteresis loop, as shown in Fig. 1, indicates a first-order phase transition. A wide meta-stable region is observed around the true phase-transition point. The melting point is adjacent to this meta-stable region. We performed the same analysis for different slit separations. Our main observation with regard to the slit separation is that the width of the hysteresis region decreases with decreasing slit separation,

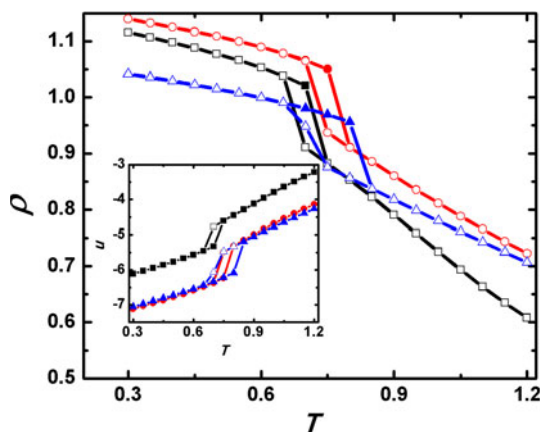


Fig. 1 Density as a function of temperature for solid and liquid phases at $P_{xx} = P_{yy} = 1.0$ for pore widths, $H = 3$, $H = 5$ and $H = 7$ for $\varepsilon_{wf} = 1$. Open symbols are representation of quenching and filled symbols for heating. Symbols triangle, circle, and square stand for $H = 7$, 5, and 3, respectively. The solid (top curve) progressively heated from $T = 0.3$ to 1.2, while the liquid (bottom) is quenched progressively from $T = 1.2$ to 0.3 where it solidifies. Inset presents the corresponding behavior for potential energy/particle (u)

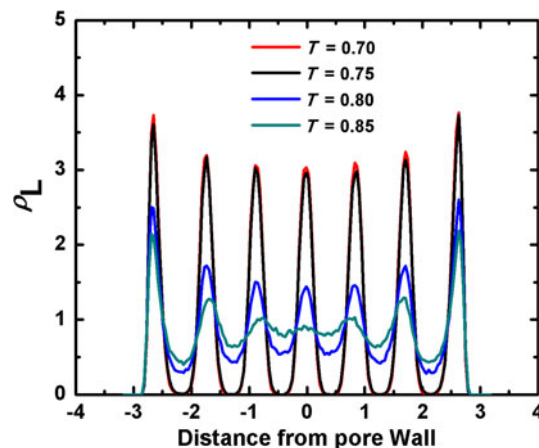


Fig. 2 Local density (ρ_L) as a function of pore distance for $H = 7.0$ and $\varepsilon_{wf} = 1.0$ for the heating case. $X = 0$ indicates center of the pore

as shown in Fig. 1. Interestingly, we also observe a clear phase transition and hysteresis for $3 \leq H \leq 5$. This result is in contrast to the previous report by Miyahara and Gubbins [20], in which hysteresis and transition are not observed below $H = 5$. The difference is primarily due to the stronger surface-fluid interaction (represented by a different potential model) used by earlier authors. The hysteresis in narrow pores $H < 5$, however, disappears with increase in surface-fluid interaction strength. This is discussed in detail later in this article.

Hysteresis is also observed for the potential energy, as shown in the inset of Fig. 1, and the hysteresis region is found to be precisely the same as that of the density. Determination of exact melting temperature or true thermodynamic transition point is not entirely feasible from the hysteresis data. However, hysteresis temperature range can indicate the region where true thermodynamic transition point might exist. We also calculated the local density at every temperature, as shown in Fig. 2. At lower temperatures, sharp distinct peaks are observed. As the temperature increases, the heights of the peaks decrease and the peaks become flatter. From the change in the peak height and shape, we can distinguish between the solid and liquid phase and also estimate approximately the melting temperature. Determination of the true melting transition point requires calculation of the grand free energy for both the solid and liquid phases. Though some work has been done in this direction using thermodynamic integration method [44] but such method requires finding a reversible path without running into intermediate phases. Unfortunately, the method fails for strong surfaces ($\alpha > 0.48$) as the path runs into first-order phase transition, at an intermediate stage [26]. Radhakrishnan et al. [26] have circumvented the above problem using Landau theory and spatially averaged order parameter.

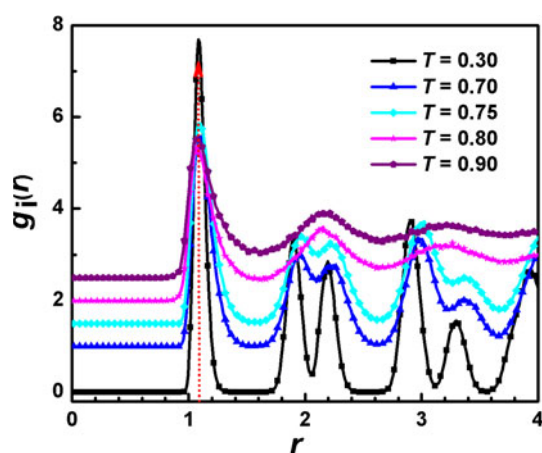


Fig. 3 In-plane pair correlation function $g_i(r)$ for $H = 7$ and $\varepsilon_{wf} = 1.0$ for the heating case. Each curve is shifted upward for better clarity. Vertical dotted line indicates position of the first peak

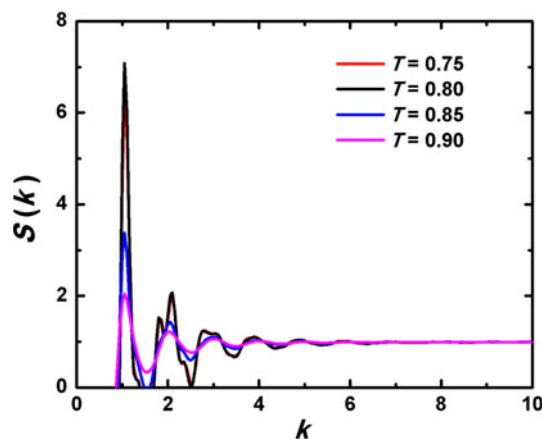


Fig. 4 Effect of temperature on the 2D structure factor, $S(k)$, of the contact layer for $H = 7.5$ and $\varepsilon_{wf} = 1.0$ for the heating case

Figure 3 presents the in-plane pair correlation function $g_i(r)$ for a contact layer of pore size 7 molecular diameters for a wide range of temperature from 0.3 to 0.9. As the temperature increases, the first peak height decreases; however, the positions of the first peaks remain constant. At lower temperatures, the second peak splits, which is an indication of a crystalline structure. At a temperature of 0.80, the second peak becomes flatter, smooth, and isotropic in nature, which indicates complete loss of crystallinity and appearance of the liquid phase. However, this temperature is not the true thermodynamic melting temperature. To use $g_i(r)$ to predict the melting temperature, a rigorous study would be required to evaluate the in-plane pair correlation function for each layer separately. However, such an approach is tedious and is not considered in this work.

Figure 4 presents the 2D structure factor $S(k)$ of the contact layer. The height of the first peak corresponds

closely to an in-plane pair correlation function. A prominent split in the second peak is observed at lower temperatures. As the temperature decreases, the rapid drop in the first peak and the split in the second peak vanish. At the melting transition, the peak height is around 4.4–5.0. From a temperature of 0.80 to 0.85, an approximately 50 % decrease in the peak height is observed. However, different layers have different peak heights at the same temperature. Hence, it is clear that the melting transition point obtained from the structure factor, which can be used for the bulk solid, is relatively difficult to predict for the confined solid.

To identify the melting point, we analyze the much-used Lindemann criterion and non-Gaussian parameter. The Lindemann parameter δ_L (Eq. 4) requires calculation of the RMS displacement of a particle (at r_i) from its equilibrium position (\mathbf{R}_i), $\langle \Delta r^2 \rangle^{1/2}$, and the averaged nearest neighbor distance. The nearest neighbor distance is the position of the first peak of the radial distribution function. The nearest neighbor distance can also be calculated using the relation $\bar{r}_{nn} = [4\Omega(T)]^{1/3} / \sqrt{2}$, where $\Omega(T)$ is the mean atomic volume at that particular temperature [29]. The distance of the first peak position of the in-plane pair correlation function remains constant over a wide temperature range. The mean-square displacement is taken for a particular time step, $\tau_0 = \sigma \sqrt{m/\varepsilon}$, which is equivalent to 610 MD time steps or 2.4 reduced time unit [39], based on Ar data. MSD is converged enough for repulsive/weak and moderately attractive walls, as shown in Fig. 5a, b, to implement the Lindemann criterion for the confined solid. Figure 5c presents the MSD versus time for a strongly attractive pore where MSD does not converge for any specific time. Hence, Lindemann criterion is not valid for such cases. We have done rigorous analysis for LJ 6-12 and LJ 9-3 walls and found that for $\varepsilon_{wf} > 8$ and $\alpha > 4$, for LJ 6-12 and LJ 9-3, respectively, this method fails and local instabilities dominate the system.

Another route for identifying the melting temperature is to track the displacement of particles from the equilibrium lattice position, which is captured by the non-Gaussian parameter, $\alpha_2(t)$ [29] (Eq. 5). As the melting temperature is approached, the non-Gaussian parameter increases as a result of strong deviation of particles from their equilibrium lattice positions, and display a single distinguishable large peak. Figure 6 presents $\alpha_2(t)$ and δ_L as a function of temperature for three cases, namely bulk, and confined states with $H = 4.5$ and 7.0. The Lindemann parameter value is calculated corresponding to the largest peak value of $\alpha_2(t)$ for the bulk fluid and found to be 0.22, which is used as the critical value. The same is used by Jin et al. [29] to estimate the melting temperature of the bulk crystal.

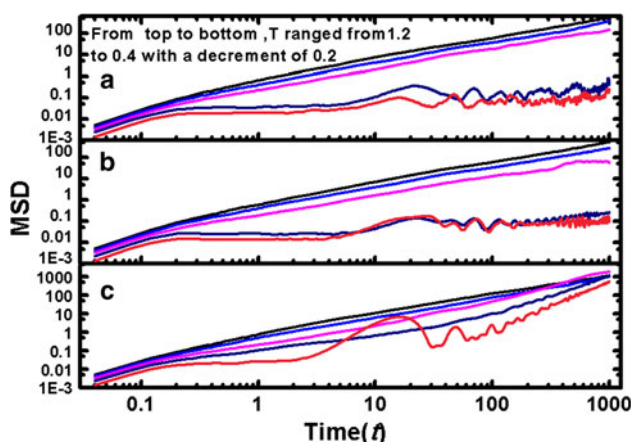


Fig. 5 Mean-square displacement (MSD) during heating the system as a function of time for $H = 8$ for different wall-fluid interactions: **a** repulsive surface (WCA), **b** moderately attractive surface ($\alpha = 2.32$), and **c** strongly attractive surface ($\alpha = 4.27$). Convergence is seen until 5 time units for repulsive and moderate attractive surface. In contrast to these for strongly attractive surface MSD does not converge even at lower temperature

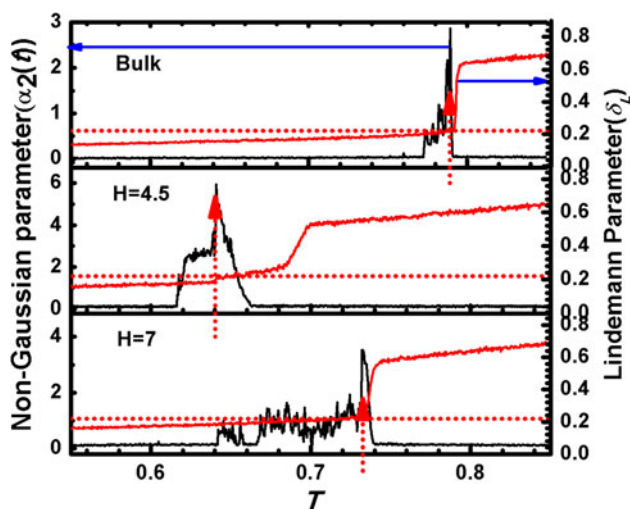


Fig. 6 The Lindemann parameter, δ_L , and non-Gaussian parameter, $\alpha_2(t)$, as a function of temperature for weak attractive pore, $\epsilon_{wf} = 1.0$. Vertical dotted arrow line from the bottom indicates the melting temperature, where non-Gaussian parameter ($\alpha_2(t)$) is maximum. Firm horizontal arrow lines represent the corresponding axes. Horizontal dotted line represents the critical Lindemann parameter for **a** bulk, **b** $H = 4.5$, and **c** $H = 7.0$

In the bulk case, our calculated melting temperature value is 0.79, as shown in Fig. 6, and is in good agreement with earlier works [45, 46]. In this work, the melting temperature of confined crystal is evaluated at the temperature where the height of the peak of $\alpha_2(t)$ is maximum. Further, we also look at the Lindemann parameter at the peak of $\alpha_2(t)$. Interestingly, Lindemann parameter based on the value at the maximum of the non-Gaussian parameter is not sensitive to the pore size, and found to be around 0.22.

The peaks in $\alpha_2(t)$ appear over a small time range for the bulk [29] and then suddenly drops to zero. In case of confinement, the time range over which the peaks exist is greater than that in the bulk system (Fig. 6b, c), as different layers melt at different temperatures as a result of the effects of confinement. This phenomenon may be considered as pre-melting, akin to that seen for the case of quenching, where different layers freeze at different temperatures and is considered as pre-freezing behavior [23, 47]. Nevertheless, $\alpha_2(t)$ displays one single distinguishable large peak which is considered to be the melting temperature. Further, at the reported pore melting temperature, significant percentage of number of particles behaves liquid-like as discussed below.

Liquid-like particles are detected by applying the Lindemann liquid-like criterion, that is, the particle possesses a Lindemann parameter greater than its critical value. Figure 7 presents the percentage of Lindemann liquid-like particles for bulk and confined cases. At higher temperatures, all the particles are in the liquid state for the confined and bulk states, as expected. However, with reduction in the pore size, the percentage of Lindemann liquid-like particle near the melting temperature increases as clearly evident from Fig. 7. At around $T = 0.3$, the percentage of Lindemann liquid-like particles for $H = 4.5$ and 7 coincide, but the values are still higher than that for the bulk state. At around the melting temperature, depicted by the vertical line, the percentage of Lindemann liquid-like particles is around 45–60 %, with the bulk value being toward the lower side. Figure 7 also indicates that the melting temperature for $H = 4.5$ should be less than that for $H = 7$ as the percentage of Lindemann particles for

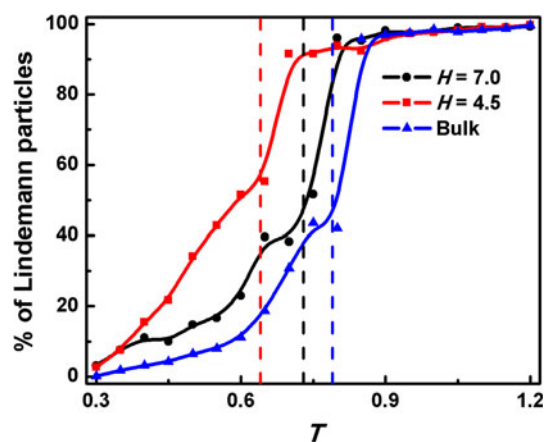


Fig. 7 Percentage of the Lindemann particles (particles possess the Lindemann parameter greater than its critical value) as a function of temperature for bulk, $H = 4.5$ and $H = 7.0$ for $\epsilon_{wf} = 1.0$. Melting temperature is lower for $H = 4.5$ as suggested by relatively higher percentage of the Lindemann particles at any temperature. Vertical dash lines represent the estimated melting temperatures

Table 1 Estimated melting temperature, T_m , for different pore size, H , with variable wall-fluid interaction strength

H	T_m					
	Wall (LJ 12-6/WCA)			Wall (LJ-93)		
	$\varepsilon_{wf} = 1$	$\varepsilon_{wf} = 3$	WCA	$\alpha = 0.481$	$\alpha = 1.362$	$\alpha = 2.32$
3.0	0.59	0.67	0.55	0.72	0.74	0.76
3.5	0.60	0.74	0.56	0.72	0.66	0.70
4.0	0.62	0.89	0.59	0.72	0.81	0.78
4.5	0.64	0.83	0.61	0.74	0.78	0.77
5.0	0.66	0.87	0.65	0.71	0.70	0.70
5.5	0.67	0.80	0.66	0.78	0.68	0.81
6.0	0.71	0.85	0.71	0.75	0.78	0.74
6.5	0.72	0.74	0.71	0.74	0.78	0.82
7.0	0.73	0.84	0.72	0.70	0.82	0.76
7.5	0.74	0.78	0.73	0.73	0.81	0.75
8.0	0.75	0.83	0.74	0.78	0.82	0.82

Bulk melting temperature at $P = 1$ is 0.79

$H = 4.5$ is higher at any temperature than that for $H = 7$. This is in line with the melting temperature based on $\alpha_2(t)$.

Table 1 summarizes the estimated melting temperatures, based on $\alpha_2(t)$, for different slit separations considered in this work. It is noted that melting temperature estimated from the $\alpha_2(t)$ is lower than that observed from the sudden change in the density-/energy-temperature plot. We notice that the solid loses its crystallinity much earlier than the temperature at which the overall order parameter such as density drops. This, however, is reflected much earlier in $\alpha_2(t)$. In case of bulk solid, the thermodynamic melting temperature and non-Gaussian melting temperature are in close proximity. This is also reflected in the narrow range of peaks in the bulk non-Gaussian plot. On the other hand, for confined solids, broad range of $\alpha_2(t)$ peaks suggests local loss of structure (as in different confined layers) much earlier than the drop in overall density of the system.

The melting temperature of a solid confined inside a weakly attractive pore at $P_{xx} = P_{yy} = 1$ is lower than that of the bulk at $P = 1$. We observe that the depression in the melting point increases with increasing reduction in the pore size as also evident from Table 1. It is also observed that the depression behavior of the melting temperature differs with pore size which is discussed in detail in Sect. 4.6.

4.2 Strongly interacting surface

We now turn our attention to strongly attractive LJ 12-6 pores, represented by the surface–fluid interaction well depth $\varepsilon_{wf} = 3.0$. Figure 8 presents plots of density versus temperature for quenching and heating. The notable difference from the case of weakly attractive pores is the

disappearance of the hysteresis loop for $H < 5$. Lack of hysteresis is an indication of superimposition of freezing and melting temperature at lower slit separation. The potential energy behavior, shown in the inset of Fig. 8, is akin to that seen for the density. The melting temperatures for strongly attractive pores based on non-Gaussian parameter with variable pore sizes are listed in Table 1. It is clear that the melting temperature is enhanced for some pore sizes, compared to the bulk value, when the pores are strongly attractive. For example, the melting temperatures for $H = 4.5$ and $H = 7.0$ are 0.83 and 0.84, respectively. The corresponding melting temperatures for the weakly attractive pores are 0.64 and 0.73. Interestingly, elevation of the melting temperature is not observed for all separations, and an oscillatory behavior is observed, as shown in Fig. 9. The oscillation in melting temperature indicates incommensurability of the crystal structures with the space available in the pores. These abnormalities in melting temperature agree well with the work of Kaneko et al. [27] and Radhakrishnan et al. [26]. Elevation of the melting temperature for confined systems has also been investigated by Klein and Kumacheva [5], and their results are in agreement with our results. Both elevation and depression in the melting temperature are observed for strongly attractive pores. The non-monotonous change in the melting temperature for strongly attractive pores is mainly caused by the structural changes in the crystal with pore size, as also reported by Kaneko et al. [27] In the case of an exact integral number of molecular diameter wall separation, the elevated melting temperature is linearly related to the wall separation, as shown in Fig. 9. Integral wall separation allows solid phase to attain a relative stable structure, in this case hexagonal lattice-based phase, as also

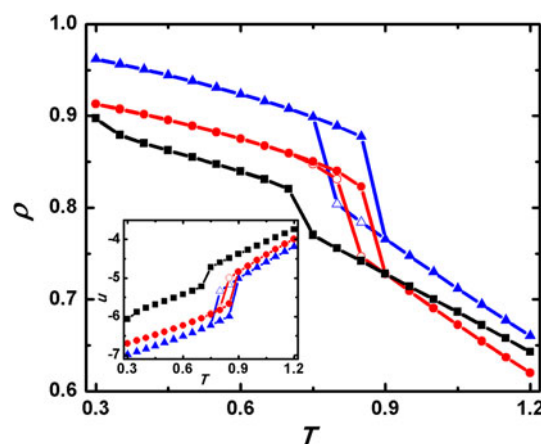


Fig. 8 Density as a function of temperature for strongly attractive pore, $\varepsilon_{wf} = 3.0$. Open symbols represent quenching and filled symbols represent heating. Symbols triangle, circle, and square represent $H = 7, 5$, and 4.5 , respectively. Inset presents the corresponding behavior for potential energy/particle (u)

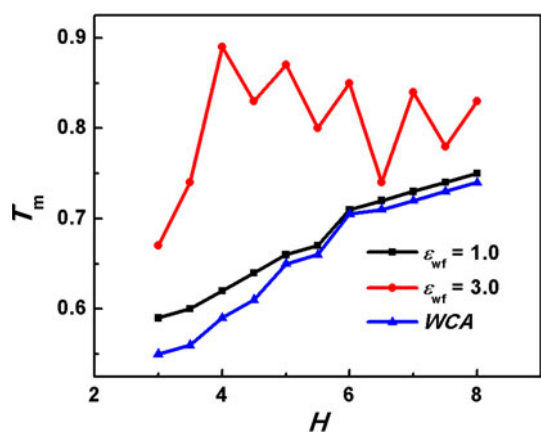


Fig. 9 Melting temperature for different wall-fluid interactions (LJ 6-12 and WCA walls) as a function of the pore size, H . The symbols *square*, *circle*, and *triangle* represent weakly attractive ($\epsilon_{wf} = 1.0$), strongly attractive ($\epsilon_{wf} = 3.0$), and repulsive (WCA) pores, respectively

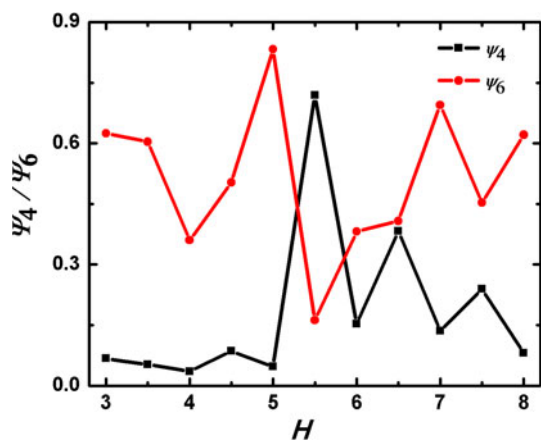


Fig. 10 In-plane order parameter of the contact layer for weakly attractive wall-fluid interaction ($\epsilon_{wf} = 1.0$) at $T = 0.5$. The behavior is seen similar for $\epsilon_{wf} = 1.0$ and WCA. See also Table 2

reflected in the bond orientational order parameter in Fig. 10; and hence, found to have higher melting temperature compared to the non-integral pore size. Free-energy calculation as a function of pore size would address the above observation more convincingly. Such an exercise is planned for a future work.

4.3 Repulsive surface

We now turn our attention to repulsive pore surfaces, modeled using the WCA potential. Using the methodologies described in this work, we calculated the melting temperatures for different pore sizes. We observed hysteresis loops for density as well as potential energy for all separations in the range 8–3 molecular diameters (figure not shown). This clearly indicates that as the pore becomes inert to repulsive, the hysteresis across the transition from a

liquid to a solid persists. As in the earlier cases, the non-Gaussian parameter is used for the estimation of the melting temperatures. The melting temperatures for $H = 4.5$ and 7 are found to be 0.61 and 0.72, which are lower than those seen for weakly attractive pores. As seen for the earlier cases of weakly and strongly attractive pores, there are considerably more Lindemann liquid-like particles for $H = 4.5$ than for $H = 7.0$, for a wide range of temperatures (figure not shown). In the case of repulsive pores, depression in the melting temperature is observed. The depression in T_m increases as the slit width decreases, as shown in Table 1 and Fig. 9. Reduction in the pore width enhances the confinement effect on the melting behavior. It is evident that the depression in T_m in repulsive pores is lower than that in weakly attractive pores. For strongly attractive pores, we observe an oscillatory behavior of the melting temperature with pore size. In the case of repulsive pores, depression in the melting temperature is observed for all pore sizes, which is not linear in nature. In fact, there appears to be two distinct regions with different slopes, and may suggest some crossover behavior with change in the pore size. This is discussed in detail in Sect. 4.6.

4.4 LJ 9-3 surface

In this study, we have used three values of $\alpha = 2.32$, 1.362, and 0.481 corresponding to wall-fluid interaction strengths (ϵ_{wf}) 0.4348, 0.255 and 0.09, respectively. Hysteresis loop for density vs. temperature is observed for all the three cases for higher wall separation, and the loop disappears at $H = 4.5$ akin to the behavior seen for the stronger wall-fluid interaction of LJ 12-6 surface (figure not shown). Potential energy behavior for cooling/heating cycle is observed to be similar in nature. Estimated melting temperatures for different pore sizes, for all three wall-fluid interaction cases, are listed in Table 1. In case of LJ 9-3 surface, $\alpha < 0.5$ wall-fluid interaction is an example of weakly attractive surface where the melting temperature under confinement is depressed relative to that of the bulk solid. However, melting temperature is found to be non-linear function of pore sizes, and shows an oscillatory behavior. LJ 9-3 surface compared to LJ 12-6 is a strong surface and even for $\alpha < 0.5$, the surface starts affecting the melting behavior dramatically compared to the weaker LJ 12-6 surface. With $\alpha > 1.0$, the surface is extremely strong and for both the two cases considered in this work, we observed depression as well as elevation in the melting temperature as shown in Fig. 11. The non-monotonic nature of melting temperature is similar to that for the stronger LJ 12-6 wall-fluid interaction. This does not agree with the results of Radhakrishnan and co-workers [26] based on Landau theory and orientational order parameter

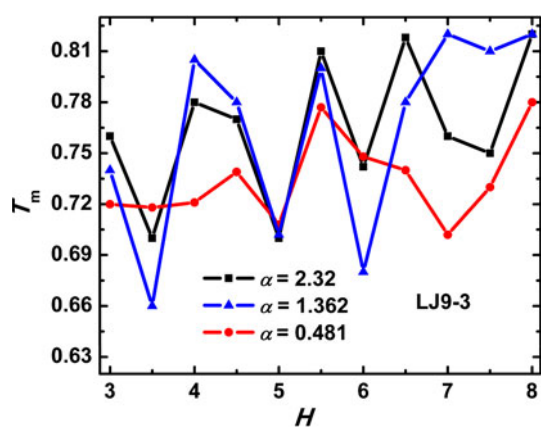


Fig. 11 Melting temperature as a function of pore size for different LJ 9-3 fluid-wall interactions

formulation, which suggest that melting temperature should elevate for $\alpha > 1.15$. This difference in observation primarily could be for two reasons. First, the current melting temperature is not the thermodynamic melting temperature. Second, the model used in this work is different from that in the work of Radhakrishnan and co-workers.

The current work based on the dynamical heterogeneity of the system suggests that local instability is seen to dominate the system particular for attractive pores, as reflected in variable structures and corresponding melting temperatures akin to the observation of Kaneko et al. [27] for $\alpha = 0.44$.

4.5 Melting temperature for different wall-fluid interaction

This work clearly suggests that the melting temperature of a confined system is usually found to shift with respect to that of the bulk. However, the magnitude and the nature of the shift (i.e., elevated or depressed) are found to depend on the wall–fluid interactions and the pore size. Both elevation and depression are observed for strongly attractive surfaces. This abnormality has also investigated by Kaneko et al. [27]. Recent simulation studies by Kaneko et al. on melting/freezing phenomena in attractive smooth slit pores (9-3 LJ) show similar types of oscillatory behavior in melting/freezing temperatures [27]. These abnormalities are the result of crystal structure variations with slit separation, and the influence of strong wall–fluid interactions. However, in the case of weakly attractive and repulsive pores, depression is observed for the pore sizes considered in this work.

Figure 12 shows the 2D CN (of the contact layer) as a function of the temperature for the case of weak LJ 6-12 pore. Figure 12 also includes 3D CN (or global) CN which

is calculated using 3D radial distribution function (i.e., considering all the layers in the system). Coordination number indicates the total number of particles directly connected with a particle. For bulk or 3D FCC crystals, the *global* CN is 12, and for 2D square and hexagonal lattices, 2D CN is 4 and 6, respectively. It is clearly observed in Fig. 12 that global CN does not indicate any structural identity (hexagonal or square lattices) except that it decreases with decrease in pore size. Further, there is a distinct change in the global CN which is similar to that seen for density against temperature behavior. However, the structural identity is displayed by the 2D CN of the contact layer, which is found to be 6, that is, hexagonal lattice structures, for all the pore sizes except for $H = 5.5$. On the other hand, for a pore size of 5.5, the structure is a square lattice with 2D CN = 4. We also rigorously studied the structure of confined crystals for all separation for already mentioned wall–fluid interaction. We present the change in crystal structure with wall separation in Table 2. The structures 3S, 3T, 4S, and 4T, etc. are different solid phases for different wall separations. Hereafter, nS indicates the n-layered solid of square-like symmetry in each layer, basically these are FCC(100) plane, and nT represents the n-layered solid of triangular- or hexagonal-like symmetry in each layer, which are mainly FCC(110) or FCC(111) plane of orientation. Figure 13 presents examples of different structures seen under confinement.

The pore size dependence of the in-plane order parameter for LJ 9-3 pores is presented in Fig. 14. We observe that the value of Ψ_6 is always greater than that of Ψ_4 for $H > 4.5$ for $\alpha = 1.362$ and 2.32. However, at a lower $\alpha = 0.481$, crystal structures appears to have periodic appearance with H . In case of lower $H < 4.5$, even for

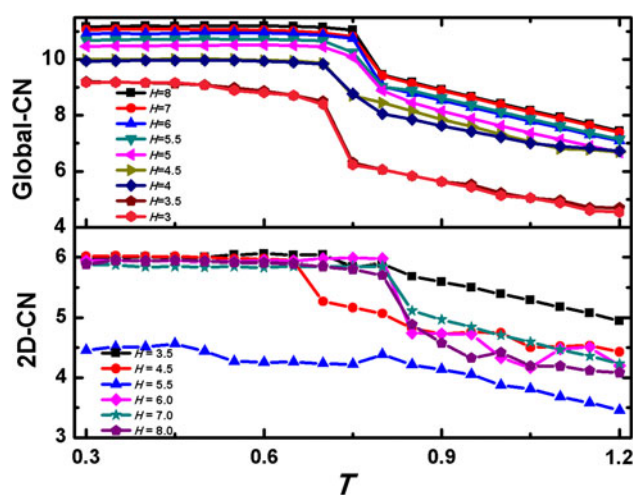


Fig. 12 In-plane coordination number (2D-CN) and global coordination number (CN) of the contact layer for weakly attractive wall-fluid interaction ($\epsilon_{wf} = 1.0$), for different pore sizes during heating run

Table 2 Crystal structures for different pore widths

<i>H</i>	Structures					
	Wall (LJ 12-6/WCA)			Wall (LJ-93)		
	$\epsilon_{wf} = 1$	$\epsilon_{wf} = 3$	WCA	$\alpha = 0.481$	$\alpha = 1.362$	$\alpha = 2.32$
3.0	3T	3T	3T	3S	3S	3S
3.5	3T	3T	3T	3T	3T	3T
4.0	4T	4T	4T	4T	4S	4S
4.5	4T	4T	4T	4T	4T	4T
5.0	5T	5T	5T	5S	5T	5T
5.5	5S	5S	5S	5T	5T	5T
6.0	6T	6T	6T	6S	6T	6T
6.5	6T	6T	6T	6T	6T	6T
7.0	7T	7T	7T	7T	7T	7T
7.5	7T	7T	7T	7T	7T	7T
8.0	8T	8T	8T	8T	8T	8T

strongly attractive pores crystal structure changes from triangular symmetry to square symmetry. For example, for $\alpha = 1.361$ at $H = 4.5$ 4T transforms to 4S at $H = 4$, and at $H = 3.5$ it is back to triangular structure 3T. This type of transformation between square and triangular lattices over

a short range of pore size was also observed by earlier workers [48]. Although we only present the in-plane bond-order data for the contact layer, all the inner layers also have the same in-plane bond-order parameter dependence on the pore size.

The type of structures observed in this work is similar to that seen by earlier workers [27, 43, 48]. In particular, we notice that the structures observed at lower H is similar to that seen by Kaneko et al. [27]; however, it differs from that seen by Ayappa et al. [48] who have employed 10-4-3 wall potential, a much stronger potential with the minima at a larger z (distance from the wall surface) distance compared to that of 9-3 potential. Further, at $H > 4$, for stronger interacting pores with $\alpha = 1.362$ and 2.32, only nT structures are seen. Similarly, for weaker 9-3 pore ($\alpha = 0.481$) and 12-6 pores, for $H > 6.0$, only nT structures are seen. In conclusion, it is clear that wall-fluid interaction affects the solid structure dramatically. In this work, it is also seen that melting temperature value of nS structures could be higher than that of nT. For example, T_m for 3S ($H = 3$) structure for the case of $\alpha \geq 1.362$ is higher than that of 3T ($H = 3.5$). On the contrary, T_m for 5S ($H = 5.5$, $\epsilon_{wf} = 3.0$) has lower T_m compared to that for 5T

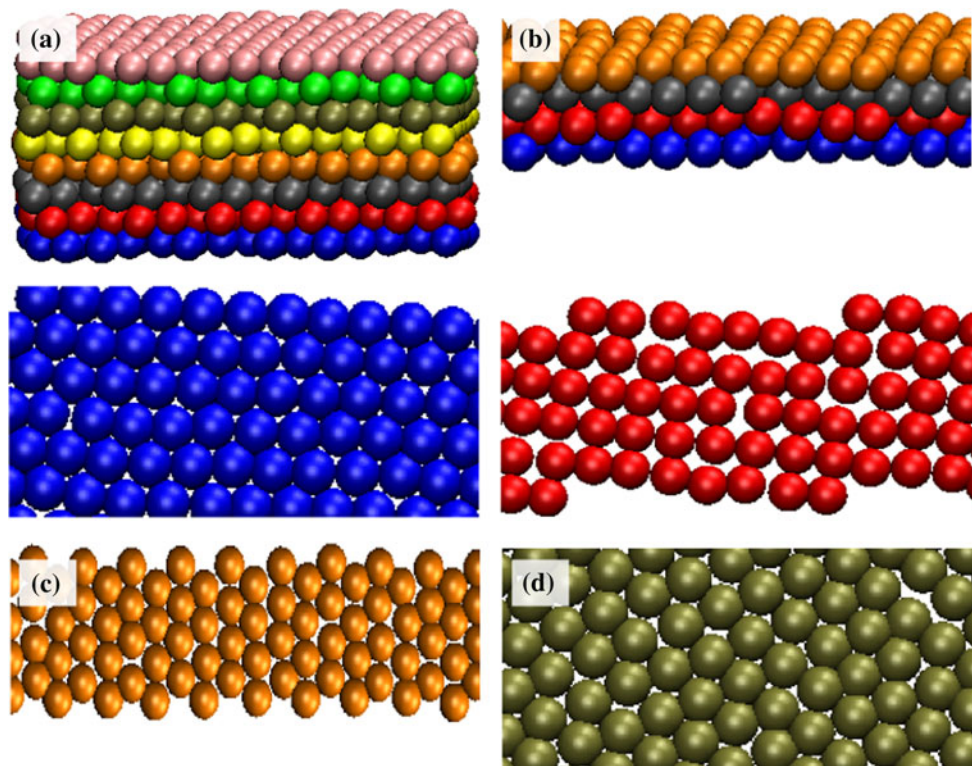


Fig. 13 Representation of snapshots for LJ particles confined in parallel slit pores. **a** The side view and the top view of the snapshot for the 8T structure at $H = 8$, $T = 0.7$, $\alpha = 2.32$; plane of orientation resemble to FCC(111) plane. **b** The side view and the top view of the snapshot for the 4S structure at $H = 4$, $T = 0.7$, $\alpha = 2.32$; plane of

orientation resemble to FCC(100) plane. **c** The top view of the snapshot for the 6T structure at $H = 6$, $T = 0.7$, $\alpha = 2.32$; plane of orientation resemble to FCC(110) plane. **d** The top view of the snapshot for the 7T structure at $H = 7.5$, $T = 0.7$, $\alpha = 2.32$; plane of orientation resemble to FCC(110) plane

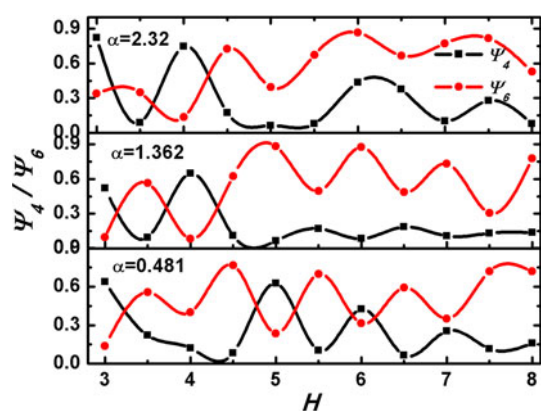


Fig. 14 In-plane order parameter of the contact layer versus H , for LJ 9-3, at $T = 0.5$ for different α values. The curves fitted to the data are guide to the eye

($H = 5.5$, $\varepsilon_{wf} = 3.0$). Kaneko et al. have seen the latter behavior more commonly in their work. The structural observation as seen in Table 2 is also supported clearly by the corresponding bond orientation order parameter which is presented in Fig. 14. Based on these results, it is not clear if a direct relation between structures and melting temperature exists.

4.6 Shift in melting temperature and crossover from 3D behavior to 2D behavior

This work visibly suggests that the melting temperature of a confined system is usually found to shift with respect to that of the bulk. However, the magnitude and the nature of the shift (i.e., elevated or depressed) are found to depend on the wall–fluid interactions and the pore size. Both

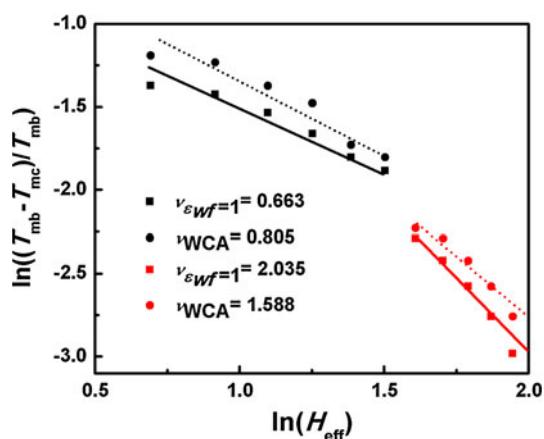


Fig. 15 Shift in melting temperature reduced by the bulk melting temperature as a function of the effective pore size, H_{eff} for weakly attractive ($\varepsilon_{wf} = 1.0$) and WCA pores. The dotted and firm lines are guide to the eye. Symbols square and circle are for weakly attractive surface and repulsive surface, respectively

elevation and depression are observed for strongly attractive surfaces. These abnormalities are the result of crystal structure variations with slit separation, and the influence of strong wall–fluid interactions. It is well known that melting behavior in 2D and 3D is not comparable. Various works have been done to understand the differences [8, 10] based on correlation functions [11]. In this work, however, we address if change in the melting temperature reflects any crossover in the nature of melting behavior as the pore size is shrunken from $H = 8$ to 3 molecular diameter. To this end, we introduce an effective wall separation as $H_{eff} = [H - (\sigma_{ff} + \sigma_{wf})/2]/\sigma_{ff}$ in order to analyze the shift in the melting temperature with respect to the bulk fluid at $P = 1$. Figure 15 presents a log–log plot of the scaled shift in T_m [$(T_{mb} - T_{mc})/T_{mb}$] against the effective wall separation. The melting temperatures in strongly attractive pores are oscillatory in nature, both elevation and depression are observed. In the case of repulsive and weakly attractive pores, we obtain the relationship $(T_{mb} - T_{mc}) = kH_{eff}^\nu$, where ν is an exponent, k is a proportionality constant, T_{mb} is the bulk melting temperature, and T_{mc} is the melting temperature under confinement. Figure 15 clearly shows two different regions with two different slopes, which depend on the wall–fluid interaction strength. The change in the slope, from $\nu > 1$ to $\nu < 1$, in both cases, that is, repulsive and weakly attractive pores, occurs at about $H = 5.5$. Typically, ν is referred to as critical exponent, and is based on the power law predicted by Fisher and Nakanishi [49] to identify the dimensionality of the state. The same has also been utilized for vapor–liquid transitions in confined geometries [50]. However, characteristic critical exponent does not exist for solid–liquid transition. Hence, the ν obtained in this work represents just a fitting variable to the data, which may be specific to the current system.

It is evident that a structural change occurs at $H = 5.5$, which may be the reason for the change in the slope of the shift in the melting point, which also occurs at $H = 5.5$, as seen in Fig. 15. Based on the above analysis, we propose that the melting behavior of a solid confined in weak/inert or repulsive pore changes from bulk-like or 3D with $\nu > 1$ to 2D with $\nu < 1$; and the critical pore size for the crossover behavior based on this study for weak to inert pore is around 5.5 molecular diameters with a structural change via a route which involves a square symmetry.

5 Conclusion

In this work, we present the melting behavior of LJ solids confined in slit pores of different pore sizes, for weak, attractive, and repulsive wall interactions. Lindemann and the non-Gaussian parameters are explored to estimate the

pore melting temperature of the confined solids. The hysteresis region that appears in the density plot is also visible in the potential energy plot. In the case of a strongly attractive surface, the hysteresis is absent for $H < 5$. In contrast, hysteresis is observed for $H = 3-8$ for weakly attractive and repulsive surfaces. The melting transition is strongly dependent on the pore size and the interactions between the wall and the fluid. In case of strongly attractive surfaces, melting temperature is found to decrease or increase, with respect to that of the bulk, depending on the pore size. The elevation in the melting temperature for integer wall separation is a linear function of the inverse of the wall separation. We observe an abnormality in the melting temperature for strongly attractive surfaces, where elevation and depression are both observed for different pore sizes. We attribute this behavior to significant changes in the crystal structure as a result of confinement and the strongly attractive surface. A depression in the melting temperature, on the other hand, is observed for the other two cases, that is, weak and repulsive pores, where the depressed temperature is a non-monotonic function of the inverse of the wall separation. A change in the slope of the plot of the shift in the melting temperature against the pore size is clearly distinguishable. Using the correlation $\Delta T_m \sim H_{\text{eff}}^{-\nu}$ for the repulsive and weakly attractive pores, the crossover behavior is analyzed. We propose that the crossover from 3D to 2D occurs around $H = 5.5$ and 2D behavior is seen with $\nu < 1.0$ and a higher pore sizes results in a 3D-like solid with $\nu > 1.0$.

The criteria used in this work utilize the overall behavior of confined crystals and hence cannot be used to identify melting temperature of confined layers. The methods further have limitation to explore melting behavior for very attractive surfaces as localized instabilities are dominant for such cases. The methods fail for $\varepsilon_{wf} > 8$ and $\alpha > 4$ for LJ 6-12 and LJ 9-3, surfaces, respectively. The reason behind the failure of the method, for strongly attractive pores, is mainly due to the instabilities in the nature of MSD and hence cannot be used for obtaining the Lindemann and non-Gaussian parameters. The instability is also seen for the bulk (where it is insignificant) or weak pores, however, that is at a larger time scale, hence such criteria are applicable for repulsive, weak, and moderately attractive pores.

Acknowledgments This work was supported by the Department of Science and Technology, Govt. of India.

References

- Zhang Z, Gekhtman D, Dresselhaus MS, Ying JY (1999) Chem Matter 11:1659
- Alcoulabi M, McKenna GB (2005) J Phys Condens Matter 17:R461
- Duffy JA, Wilkinson NJ, Fretwell HM, Alam MA (1995) J Phys Condens Matter 7:L27
- Unruh KM, Huber TE, Huber CA (1993) Phys Rev B 48:9021
- Klein J, Kumacheva E (1995) Science 269:816
- Gelb LD, Gubbins KE, Radhakrishnan R, Sliwinski-Bartkowiak M (1999) Rep Prog Phys 62:1573
- Alba-Simionesco C, Coasne B, Dosseh G, Dudziak G, Gubbins KE, Radhakrishnan R, Sliwinski-Bartkowiak M (2006) J Phys Condens Matter 16:15
- Murray CA, Winkle DHV (1987) Phys Rev Lett 58:1200
- Tang Y, Armstrong AJ, Mockler RC, Sullivan WJO (1989) Phys Rev Lett 62:2401
- Murray CA, Sprenger WO, Wenk RA (1990) Phys Rev B 42:688
- Murray CA, Sprenger WO, Wenk RA (1990) J Phys Condens Matter 2:SA385
- Warnock J, Awschalom DD, Shafer MW (1986) Phys Rev Lett 57:1753
- Klein J, Perahia D, Warburg S, Fetters LJ (1991) Nature 352
- Klein J, Kumacheva E, Perahia D, Mahalu D, Warburg S (1994) Faraday Spec Discuss Chem Soc 98
- Delogu F (2006) Phys Rev B 73:184108
- Delogu F (2006) J Phys Chem B 110:12645
- Delogu F (2006) J Phys Condens Matter 18:5639
- Huang HC, Kwak SK, Singh JK (2009) J Chem Phys 130:164511
- Schmidt M, Löwen H (1996) Phys Rev Lett 76:4552
- Miyahara M, Gubbins KE (1997) J Chem Phys 106:2865
- Maddox MW, Gubbins KE (1997) J Chem Phys 107:9659
- Radhakrishnan R, Gubbins KE (1999) Mol Phys 96:1249
- Sliwinski-Bartkowiak M, Dudziak G, Sikorski R, Gras R, Radhakrishnan R, Gubbins KE (2001) J Chem Phys 114:950
- Coasne B, Czwartos J, Gubbins KE, Hung FR, Sliwinski-Bartkowiak M (2005) Adsorption 11:301
- Radhakrishnan R, Gubbins KE, Sliwinski-Bartkowiak M (2002) J Chem Phys 116:1147
- Radhakrishnan R, Gubbins KE, Sliwinski-Bartkowiak M (2000) J Chem Phys 112:11048
- Kaneko T, Mima T, Yasuoka K (2010) Chem Phys Lett 490:165
- Koga K, Tanaka H (2005) J Chem Phys 122:104711
- Jin ZH, Gumbsch P, Lu K, Ma E (2001) Phys Rev Lett 87:055703
- Granato AV, Joncich DM, Khonik VA (2010) Appl Phys Lett 97:171911
- Born M (1939) J Chem Phys 7:591
- Radhakrishnan R, Gubbins KE (1999) J Chem Phys 111:9058
- Hansen JP, Verlet L (1969) Phys Rev 184:151
- Gotze W, Lüicke M (1976) J Low Temp Phys 25:671
- Broughton JQ, Gilmer GH, Weeks JD (1982) Phys Rev B 25:4651
- Ranganathan S, Pathak KN (1992) Phys Rev A 45:5789
- Monson PA, Kofke DA (2000) Adv Chem Phys 115:113
- Lindemann FA (1910) Z phys 11:609
- Hoang VV (2011) Philos Mag 91(26):3443
- Stillinger FH (1995) Science 267:1935
- Cailloi JM, Levesque D, Weis JJ, Hansen JP (1982) J Stat Phys 28
- Plimpton SJ (1995) J Comp Phys 117:1
- Kaneko T, Yasuoka K, Zeng XC (2012) Mol Sim 38:373
- Dominguez H, Allen MP, Evans R (1999) Mol Phys 96:209
- Hoef MAvd (2000) J Chem Phys 113:8142
- Eike DM, Brennecke JF, Maginn EJ (2005) J Chem Phys 124:014115
- Morishige K, Kawano K (2000) 104:2894
- Ayappa KG, Ghatak C (2002) J Chem Phys 117:5373
- Fisher ME, Nakanishi H (1981) J Chem Phys 75:5857
- Singh SK, Singh JK, Kwak SK, Deo G (2010) Chem Phys Lett 494:182